# RESEARCH ARTICLE

**Correspondence to:**
S. Xu,
xussui@umich.edu

# Solar wind electron precipitation into the dayside Martian upper atmosphere through the cusps of strong crustal fields

**Shaosui Xu[1], Michael W. Liemohn[1], and David L. Mitchell[2]**

[1]Department of Atmospheric, Oceanic, and Space Sciences, University of Michigan, Ann Arbor, Michigan, USA, [2]Space Sciences Laboratory, University of California, Berkeley, California, USA

**Abstract** Measurements made by the magnetometer/electron reflectometer on board the Mars Global Surveyor spacecraft have shown spatially localized enhancements in electron fluxes over the strong crustal fields on both the dayside and night, which are used to identify the cusps in between the closed magnetic fields. This paper provides a comprehensive statistical study on the occurrence rate of dayside solar wind/magnetosheath precipitation over the strong crustal fields. Also, the occurrence rate's dependence on the magnetic elevation angles and the solar zenith angle is presented. A seasonal variation of the precipitation is also expected and found, due to both the tilt and the orbital eccentricity of Mars. The maximum occurrence rate is 40%, when the solar zenith angles are small and the magnetic fields are nearly vertical. Finally, the energy flux deposition of the solar wind electrons is calculated as well, which is 0.1%–2% of solar EUV flux input.

## 1. Introduction

Crustal magnetic anomalies at Mars have been discovered by the magnetometer/electron reflectometer (MAG/ER) on board the Mars Global Surveyor (MGS) spacecraft [*Acuña et al.*, 1998], and their interaction with interplanetary magnetic field (IMF) results in complex magnetic field topology [e.g., *Brain et al.*, 2003, 2007; *Harnett and Winglee*, 2005, *Ma et al.*, 2014]. Studies have been conducted on how the crustal magnetic fields affect localized plasma processes [e.g., *Withers et al.*, 2005; *Nielsen et al.*, 2007; *Krymskii et al.*, 2003; *Brain et al.*, 2010]. Open magnetic field lines, resulting from the connection between the IMF and crustal fields, have been discovered and confirmed by several studies via identifying solar wind/magnetosheath electron precipitation [e.g., *Mitchell et al.*, 2001; *Liemohn et al.*, 2003; *Brain et al.*, 2005; *Dubinin et al.*, 2008a, 2008b]. Furthermore, *Brain et al.* [2007] discussed how often the fields above different geographic regions were open/closed by analyzing electron pitch angle distributions. These open field lines allow ionospheric photoelectrons to escape into space [e.g., *Frahm et al.*, 2006a, 2006b; *Liemohn et al.*, 2006, 2007] and solar wind/magnetosheath electrons to precipitate into the Martian upper atmosphere. The precipitation of superthermal electrons into the Martian atmosphere can cause heating [e.g., *Krymskii et al.*, 2002, 2004], excitation (especially aurora on the nightside [e.g., *Bertaux et al.*, 2005; *Brain et al.*, 2006; *Leblanc et al.*, 2008]) and dissociation and ionization [*Schunk and Nagy*, 2000].

*Mitchell et al.* [2001] identified solar wind/magnetosheath electron precipitation through open magnetic field lines on the nightside, resulting in the spikes of high electron fluxes in between plasma voids (whose energy spectra are near-instrument background level flux, a feature of closed magnetic fields). Also, *Dubinin et al.* [2008a] observed spatially organized narrow spikes in regions of strong crustal field on the Martian nightside by the Analyzer of Space Plasma and Energetic Atoms 3 experiment [*Barabash et al.*, 2006] on board the Mars Express (MEX) spacecraft. Furthermore, a systematic study of the nightside electron precipitation's geographic pattern and dependence on solar wind conditions was conducted by *Lillis and Brain* [2013]. On the dayside, *Brain et al.* [2005] studied how often solar wind/magnetosheath electrons penetrate below 400 km by analyzing the omnidirectional electron fluxes measured by MGS and then concluded the hemispherical asymmetry and seasonal variation of the altitude of the magnetic pileup boundary (MPB), also its dependence on the IMF directions. In particular, a higher probability of magnetosheath plasma intrusion was observed in some patches surrounded by closed strong crustal fields, where field lines more likely connect to the IMF.
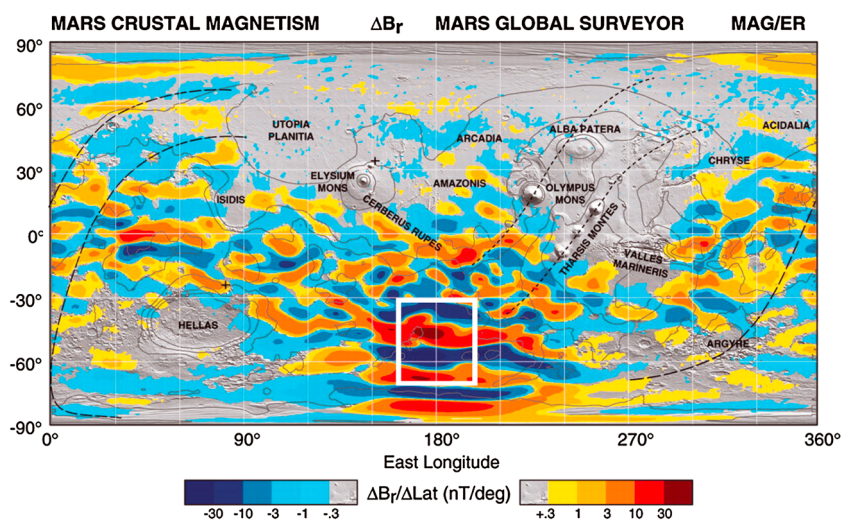
Connerney J E P et al. (2005) Proc. Nati. Acad. Sci. USA;vol. 102, no. 42:14970-14975

**Figure 1.** Radial *B* field of Mars [*Connerney et al.*, 2005], with the white box representing the geographic selection boundaries of this study, also Figure 1 of *Trantham et al.* [2011]. Copyright (2005) National Academy of Sciences, USA.

In this study, we take a statistical approach to identify solar wind/magnetosheath electrons and ionospheric photoelectrons and determine the occurrence rate of dayside solar wind/magnetosheath electron precipitation over strong crustal fields. In addition, we investigate the dependence of the occurrence rate on the magnetic elevation angle, as more vertical magnetic field lines have a higher chance to be open at MGS altitudes. The occurrence rate also depends on the solar zenith angle (SZA), as the normal solar wind dynamic pressure decreases from subsolar point to terminator. Furthermore, although solar photon absorption is certainly the largest source of energy input to the Martian upper atmosphere, quantification of how superthermal electrons' energy input compares to solar input has not been done. This new approach also allows us to quantify the energy flux deposition of solar wind/magnetosheath electrons into the dayside Martian upper atmosphere and compared it with solar flux input.

## 2. Methodology

The MAG was operated at $405 \pm 36$ km altitude and locked to 0200/1400 local time (LT) during its mapping phase. Together with vector magnetic field data measured by MAG, the ER onboard MGS measured superthermal electron angular distributions with an energy range 10 eV to 20 keV [*Acuña et al.*, 1992; *Mitchell et al.*, 2001]. Every 2–8 s, the ER recorded electron fluxes in sixteen $22.5° \times 14°$ sectors, which spanned the entire $360° \times 14°$ field of view (FOV). With both the vector magnetic field and the electron angular distribution measured, the FOV can be converted into pitch angles [*Mitchell et al.*, 2001, equation (1)]. As the MGS spacecraft did not spin, the ER can only provide 2-D pitch angle distributions (PADs) rather than a full 3-D velocity space distribution and the sampled width of the PAD also varies according to the orientation of the ambient field with respect to the ER detection plane. In other words, if the magnetic field was in the plane of the instrument field of view, all 180° were sampled, but if the magnetic field was perpendicular to this plane, only pitch angles near 90° were sampled [see *Liemohn et al.*, 2006, Figure 9]. It is important to notice this possible bias in the number of samples for the different pitch angles.

This study focuses on the solar wind/magnetosphere electron precipitation through cusps, where the magnetic topology changes from one closed loop arch to the next, over the strong crustal fields. Hence, we confined the data to a region between 30° to 70° south latitude and 160° to 200° east longitude, as shown as the white box in Figure 1, where the strong crustal fields consist of well-defined loop structures (also Figure 1 of both *Connerney et al.* [2005] and *Trantham et al.* [2011]). The cusps are located between the closed magnetic field loops and are more likely found when the field line is more vertical. Therefore, any open magnetic field within the cusp region is more likely to be seen at large magnetic elevation angle at the MGS altitude. Another constraint, an absolute magnitude elevation angle observed by MGS
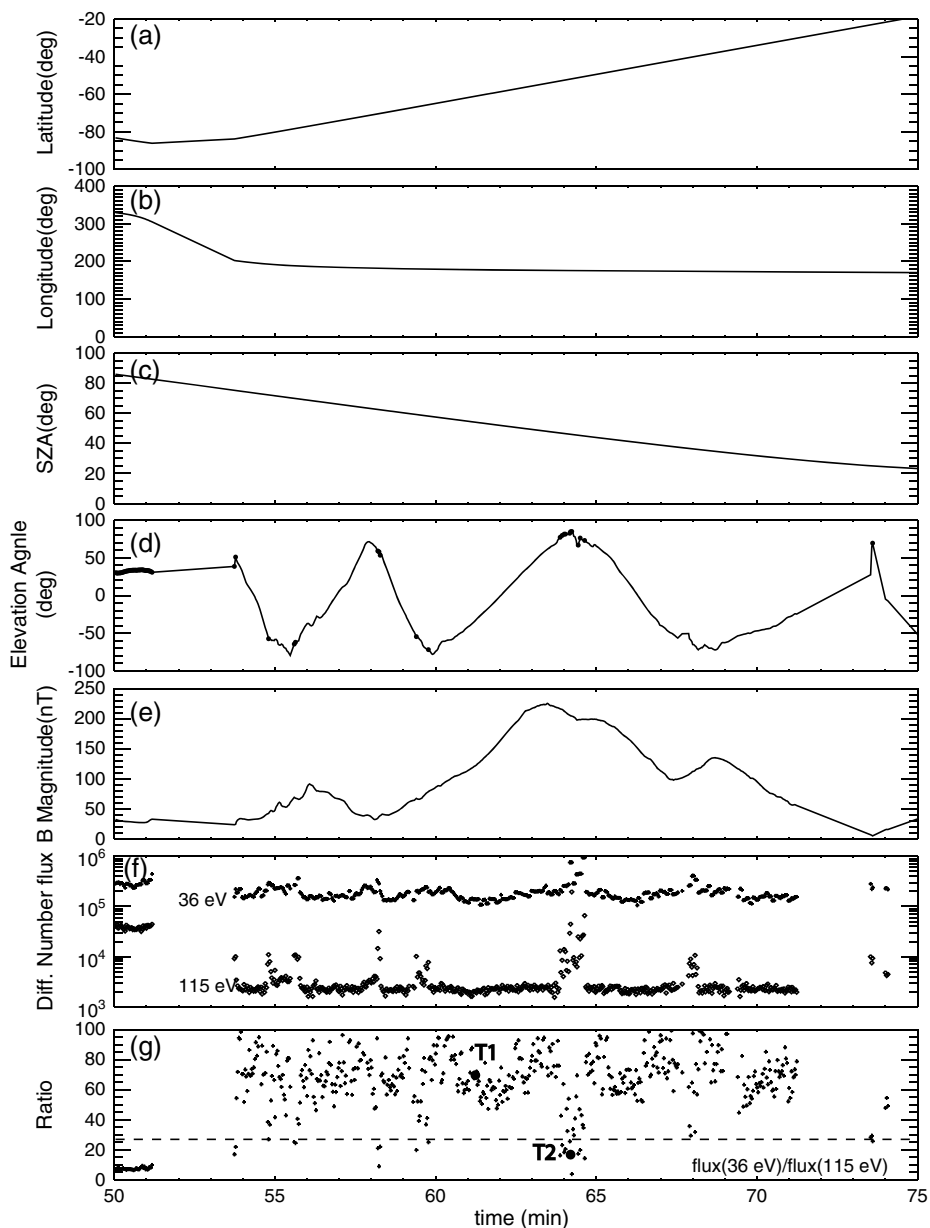
**Figure 2.** One orbit example: MGS data for 15 January 2004, the *x* axis is the time in minutes, starting from UT 10:00:00. Shown are (a) MGS location over Mars in latitude; (b) MGS location over Mars in east longitude; (c) MGS solar zenith angle; (d) the elevation angle of the magnetic fields; (e) the magnitude of the magnetic fields; (f) differential number flux (# eV$^{-1}$ cm$^{-2}$ s$^{-1}$ sr$^{-1}$) for 36 eV and 115 eV two energy channels at PA 150°–160°; (g) the flux ratio of the two energy channels shown in Figure 2e. The dashed line in Figure 2g is a ratio of 27. The black dots in Figure 2d are when the flux ratios are below this dashed line. The two black dots in Figure 2g are two points used for Figure 3.

MAG greater than 45°, is applied, because the chance to observe solar wind/magnetosheath electrons at smaller angles is very low [*Liemohn et al.*, 2003; *Trantham et al.*, 2011]. A minimum magnetic field strength of 35 nT to ensure strong crustal fields and a maximum SZA of 90° to select dayside data are also applied.

To separate electrons moving toward/away from the planet, "modified pitch angles" are used in this study, flipping the pitch angles if the magnetic field points toward the planet (negative magnetic elevation angles), as was done by *Xu et al.* [2014]. For example, if **B** points toward the planet, the original pitch angle of 10° would now be 170°. In other words, electrons at pitch angle 0°–90° (90°–180°) always have a velocity component away from (toward) the planet.
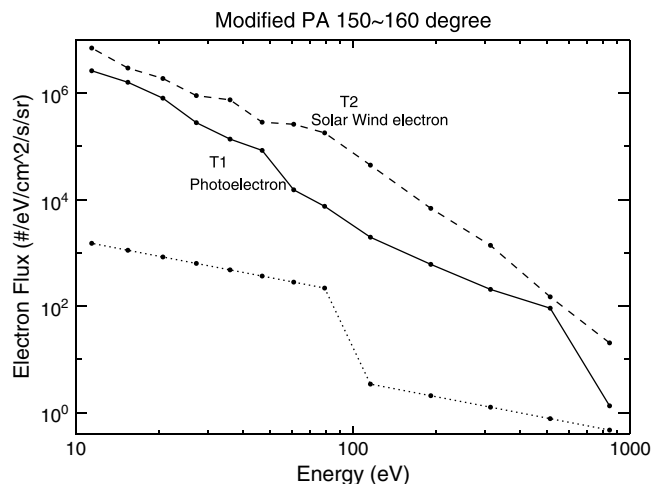
**Figure 3.** Energy spectra (differential number flux at PA 150°–160° against energy in eV) of the two black dots in Figure 2. The solid line is for the higher ratio (T1), while the dashed line is for the lower ratio (T2). The dotted line is the instrumental background flux.

## 3. Results

In this section, we first described the method used to identify solar wind/magnetosheath electrons (section 3.1) and then calculated the occurrence rate of the solar wind/magnetosheath electron precipitation (section 3.2). Then the occurrence rate's dependence on the magnetic elevation angle (section 3.3) and the solar zenith angle (section 3.4) is also discussed. Finally, the energy flux deposition of solar wind/magnetosheath electrons is presented in section 3.5.

### 3.1. Identifying Solar Wind Electrons

Solar wind/magnetosheath electrons have been previously identified on the dayside by studies [e.g., *Liemohn et al.*, 2003] of MGS observations. Figure 2 shows the measurements of one orbit of MGS on 15 January 2004, starting at universal time (UT) 10:50:00. From around UT 10:54 to UT 11:11, MGS flew through the strong crustal fields (east longitude 190° to 170°, south latitude 80° to 30°) on the dayside (SZA 75° to 30°). The strong crustal fields can usually be identified by the large variation of the elevation angles of the magnetic field, shown in Figure 2d, and the large magnitude (a few tens of nT to over 200 nT seen in Figure 2e). Figure 2f shows the differential number flux (# eV$^{-1}$ cm$^{-2}$ s$^{-1}$ sr$^{-1}$) for 36 eV and 115 eV two energy channels at pitch angle (PA) 150°–160°. Within the first minute, MGS was around the terminator (SZA ∼ 90°), and the fluxes for both channels are relatively high and then drop significantly when the satellite flew through the crustal fields as the electron population switched from solar wind/magnetosheath electrons, with higher fluxes, to the ionospheric originated photoelectrons, with lower fluxes. The flux drop for the two channels are different, a factor of ∼ 2 decrease for the 36 eV channel and a much larger (over an order of magnitude) decrease for the 115 eV channel. This different amount of flux drop is due to one of the photoelectrons' features: the sharp drop of photoelectron fluxes around 60 eV, the so-called "knee" in the energy spectra (due to the sharp drop in solar photons below 15 nm) while for solar wind/magnetosheath electron spectra, the decrease of electron fluxes is much slower [e.g., *Fox and Dalgarno*, 1979; *Mantas and Hanson*, 1979; *Crider et al.*, 2000; *Mitchell et al.*, 2001; *Liemohn et al.*, 2003]. In other words, the flux ratio of the 36 eV and 115 eV channels is much higher for photoelectrons than solar wind/magnetosheath electrons, as shown in Figure 2g.

However, the fluxes jump back to their original high values occasionally during the flight over the strong crustal fields (Figure 2f), such as at UT 10:58 and UT 11:04. Magnetic fields with near 90° elevation angles are more likely to be connected to the IMF, thus a higher possibility of solar wind/magnetosheath electrons entering the Martian atmosphere. These spikes seem to correspond to high elevation angles by comparing Figures 2d and 2f, thus considered as solar wind/magnetosheath electron precipitation through the magnetic field lines inside the cusps on the dayside. Furthermore, data points with flux ratios below the dashed line in Figure 2g (ratio = 27) are marked with black dots in Figure 2d, marked as T1 and T2. Over the strong crustal fields (UT 10:54–11:11), the low flux ratios are seen at elevation angles near 90°, as expected.
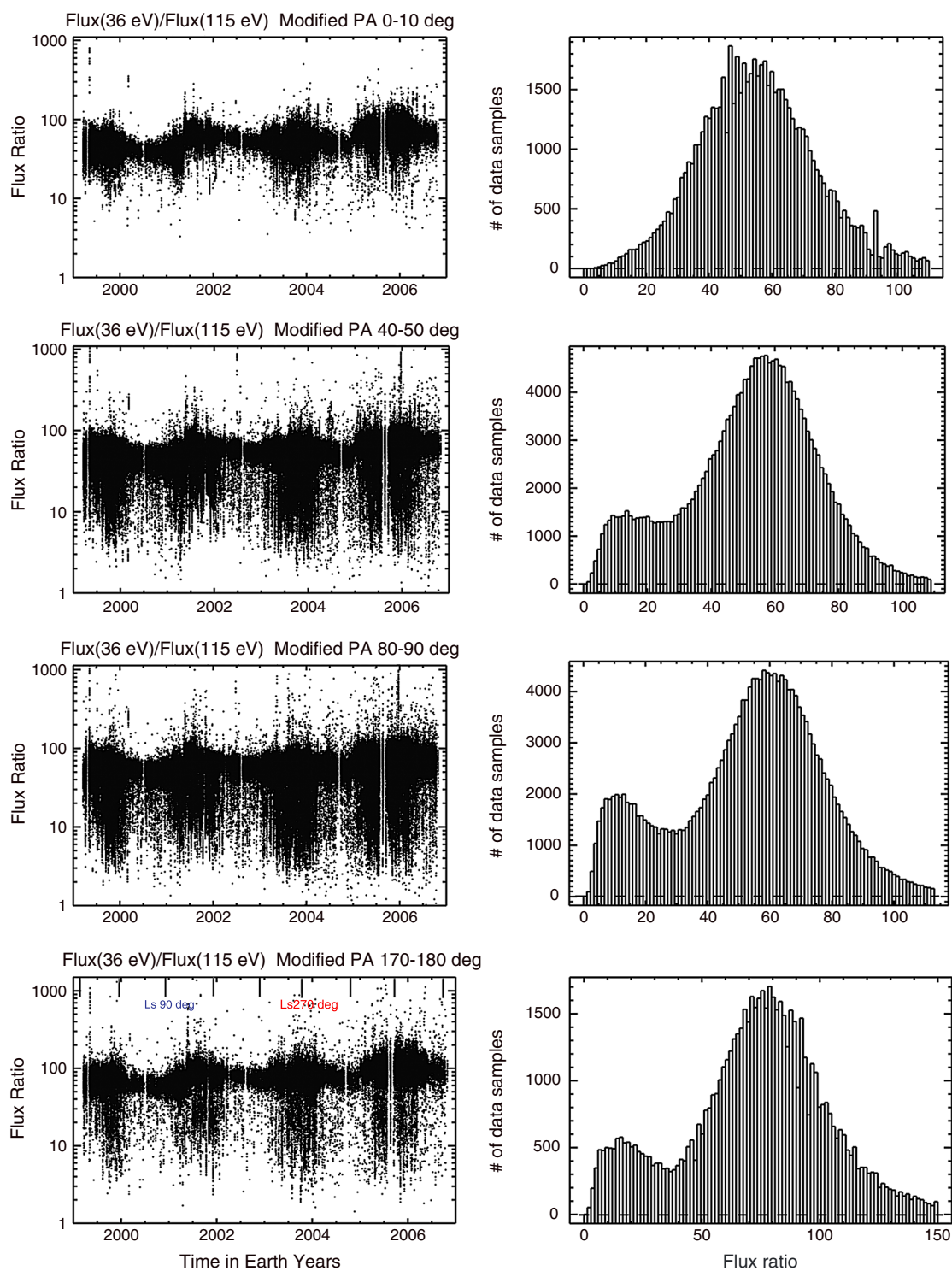
The basic idea of this study is to separate solar wind/magnetosheath electrons and ionospheric photoelectrons by utilizing the different flux ratios of the two populations, with one energy channel smaller than the energy of this knee, e.g., 36 eV, and one channel larger, e.g., 115 eV. To further validate this idea, the energy spectra (differential number flux at PA 150°–160° against energy in eV) of two data points with a high and low flux ratio (T1 and T2 in Figure 2g, respectively) are shown in Figure 3. The solid line is for the higher ratio (∼ 70, T1), while the dashed line is for the lower ratio (∼ 20, T2), with the dotted line showing

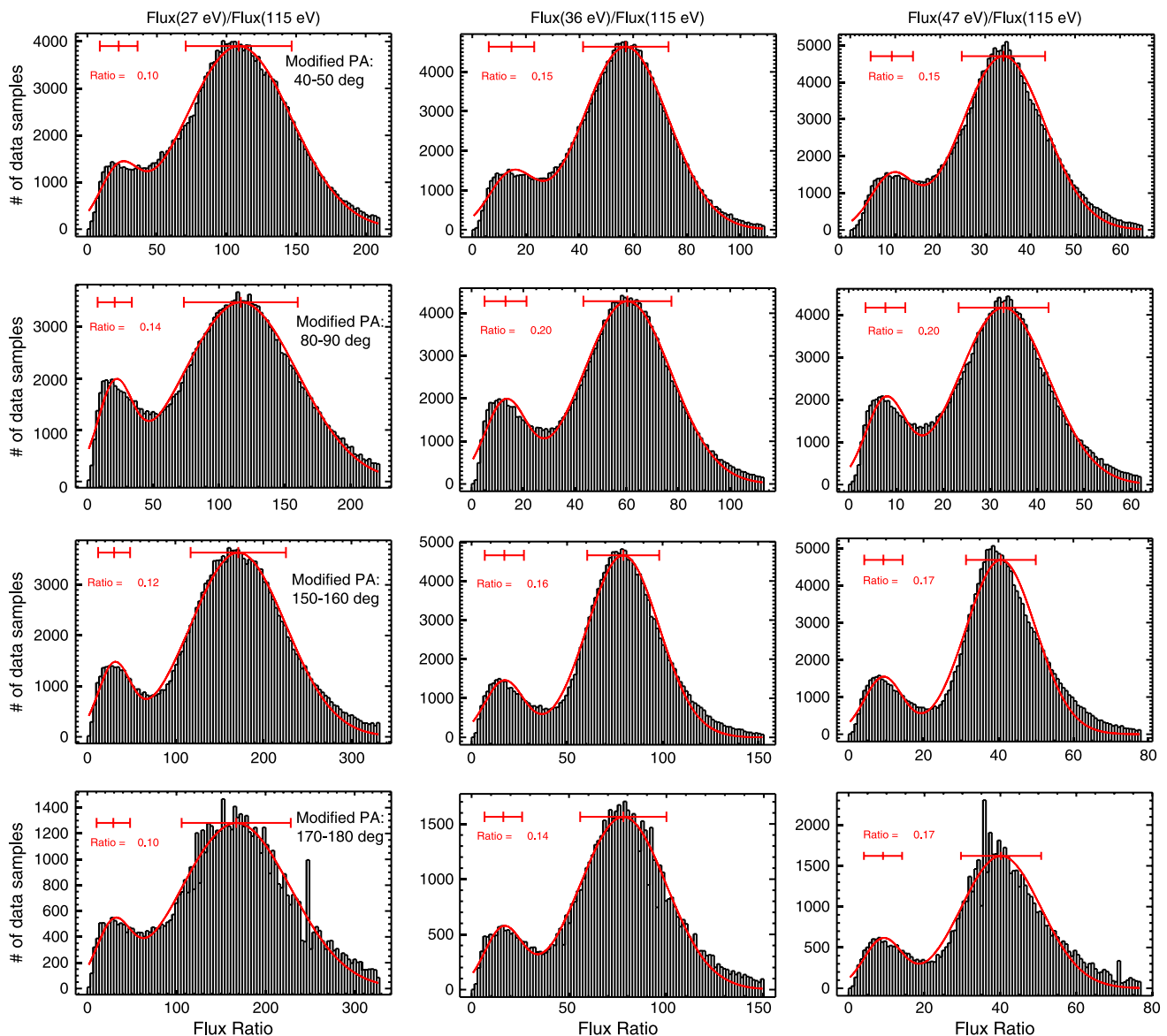**Figure 4.** (left) The ratio of electron fluxes at 36 eV and at 115 eV against time; (right) the histogram of the left plots. Each row is for different modified pitch angles, (top to bottom) 0°–10°, 40°–50°, 80°–90°, and 170°–180°. The blue and red ticks in the lowest left panel mark solar longitude (Ls) of 90° and 270°, i.e., Martian southern winters and summers, respectively.

**Figure 5.** The three columns are the histogram plots of the flux ratios of three energy pair: (left) 27 eV and 115 eV, (middle) 36 eV and 115 eV, and (right) 47 eV and 115 eV. The four rows are for four pitch angles, (top to bottom) 40°–50°, 80°–90°, 150°–160°, and 170°–180°. The red lines are fittings to each plot. Also, the sample ratio of the two populations are also shown at the upper left corner in each plot. In addition, the red bars at the top of each panel mark the flux ratio where the fitted Gaussian distribution peaks, along with the standard deviation of each Gaussian-like distribution.

the instrumental background flux. The energy spectrum for T1 shows some ionospheric photoelectron features: the knee around 60 eV and also the sharp decrease of fluxes around 500 eV due to the extremely small source term for energies above. However, for T2, none of these features are seen. This characteristic difference in energy spectra for high and low flux ratios holds for all the examples that we individually examined. Hence, it is reasonable to distinguish the two populations by analyzing the statistical results of their flux ratios over the whole mapping phase of MGS, from Earth year 1999 to 2007.

Figure 4 (left) is the ratio of electron fluxes at 36 eV and at 115 eV against time, while Figure 4 (right) is the histogram of the left plots. Each row is for different "modified pitch angles," from top to bottom: 0°–10°, 40°–50°, 80°–90°, and 170°–180°. As shown in the first row of Figure 4, when the pitch angle is 0°–10°, the ratio is centered at a few tens and the distribution over 7 years is an approximately Gaussian distribution, peaked at a flux ratio ∼50. Since this peak flux ratio is more closer to that of T1 (∼70), i.e., the photoelectron sample, these electrons are likely fresh ionospheric photoelectrons, propagating upward. As the pitch
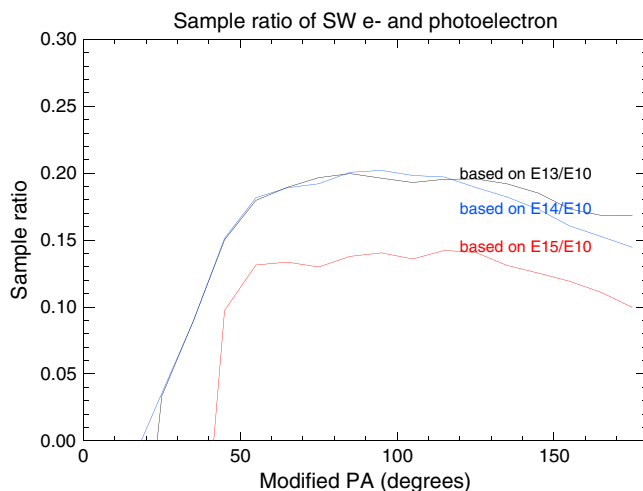
**Figure 6.** Sample ratio of the two populations against modified pitch angles. The three colors are for three energy pairs: 27 eV and 115 eV (red), 36 eV and 115 eV (blue), and 47 eV and 115 eV (black).

angle increases, especially for the downward pitch angle bins, such as 170°–180°, ratios extend below 20, while the histogram starts to show a bimodal distribution. A Gaussian-like distribution centers at a ratio of around 60, which resembles the population seen above at upward field-aligned pitch angles as ionospheric photoelectrons. In addition, another peak of a lower ratio, around 10, is also shown, indicating another population of electrons, i.e., solar wind/magnetosheath electrons. This population change at different pitch angles (PAs) can be explained as below. Over the strong crustal field, electrons that move along the magnetic field line away from the planet (PA < 90°) most likely originated in the ionosphere. For pitch angles greater than 90°, electrons either originated in the ionosphere in the conjugate leg of the same magnetic field loop or originated in the solar wind/magnetosheath, precipitating into the atmosphere through an open magnetic field line (most likely inside the cusps). The second population, as shown in PA 40°–50° of panels in the second row, is possibly reflected solar wind/magnetosheath electrons due either to the collisional scattering with the neutral atmosphere and/or charged particles or to the magnetic mirroring effect as the magnetic field strength increases when closer to the planet above the strong crustal field regions. The existence of these reflected electrons suggests at a loss cone of < 40°. Notice that the $y$ ranges of the histogram plots in Figure 4 are different. There are fewer data samples at more field-aligned pitch angles (∼0° or 180°) than more perpendicular pitch angles (∼90°), due to the 2-D FOV (field of view) of the instrument.

### 3.2. Precipitating Solar Wind Electron Occurrence Rate Calculation

In order to obtain the ratio of the two populations and the cutoff to separate them, the bimodal distribution is treated as the addition of two Gaussian distributions. Even though some distributions of the left population, i.e., solar wind electrons, are not quite Gaussian-like, this Gaussian approximation is convenient and still reasonable. A new function that consists of two Gaussian functions is fitted to the bimodal distribution, with three to-be-fitted variables (the amplitude, the position of the peak, and the standard deviation) to each function, as shown in Figure 5. The basic idea of this fitting is to compute a nonlinear least squares fit to this new function. The three columns of Figure 5 show the histogram plots of the flux ratios between the energy bins centered at 27 eV and 115 eV, 36 eV and 115 eV, and 47 eV and 115 eV, respectively. Three energy pairs are examined here to show if their results are similar, therefore if this method delivers reliable performance. The four rows are for four pitch angles: 40°–50°, 80°–90°, 150°–160°, and 170°–180°. The red lines are the fits to the distributions. The red bars at the top of each panel of Figure 5 show the mean flux ratio, i.e., where the fitted curve peaks, and the standard deviation for each fitted Gaussian distribution. The far apart red bars for two distributions suggest that the bimodal distribution indeed consists of two populations.

Another significant and meaningful quantity that can be extracted from Figure 5 is the occurrence rate of the solar wind electrons' precipitation into the Martian upper atmosphere through cusps, which essentially is the percentage of the number of identified solar wind electron measurements out of the total measurements. Here the ratio of the number of the measurements of the two populations is first calculated, given in the left upper corner of each plot in Figure 5. It is obtained by integrating each fitted Gaussian function from 0 to positive infinity (the negative part is neglected because of the lack of physical meaning) and then acquire the ratio of the two obtained integrals. Figure 6 shows how this ratio changes with pitch angle based on the distributions of three pairs of the flux ratios in Figure 5, highlighted by different colors. The three lines share the same trend: the plunging of the ratio at more field-aligned upward PAs, 0°–40°,

due to the lack of solar wind electrons; then the near constant value at PA 40°–120°; finally, a slow decrease at the downward field-aligned PAs. For the first few upward pitch angle bins, the sample ratio is about 0.

The highest possibility of solar wind electron precipitation happens at PA near 90°. There are two possible explanations. First, it is possible that solar wind electrons are more likely to be found when the pitch angle distribution is only partially sampled. As said in section 2, the instrument only has a 2-D FOV so that only part of the pitch angles, near 90°, are sampled when the magnetic field line is out of the plane of the instrument. As the data selected for this study are confined within a box of loop-structure strong crustal fields, the magnetic field (while not always true) is more likely north-south directed, thus in the plane of the instrument as MGS is flying northward in the dayside. The chance of magnetic field lines being twisted out of this plane due to the reconnection with the IMF is rather high as the IMF usually has an east-west component. As a result, partially sampled PADs, centered at PA ∼90°, may hint at a higher possibility of open magnetic field lines through which solar wind electrons can precipitate into the Martian atmosphere. Second, it seems that the measured pitch angle distribution of electron fluxes at the high-energy range at 2 P.M. is more isotropic than expected [e.g., *Liemohn et al.*, 2003; *Brain et al.*, 2007] over the strong crustal fields, which is actually identified as photoelectrons by *Brain et al.* [2007]. The more isotropized pitch angle distribution of photoelectrons at 115 eV, compared to a classic source cone distribution, decreases the flux ratio for perpendicular pitch angles, due to a larger denominator, and increases the flux ratio for field-aligned pitch angles, due to a smaller denominator. As a result, photoelectrons are more easily miscounted as solar wind electron samples at perpendicular pitch angles due to the smaller flux ratio while the field-aligned pitch angles are not affected.

Despite the similarity of the three lines, while the ratios between solar wind electron samples and photoelectron samples derived from the distribution of the flux ratio of energy channels 36 eV and 115 eV (denoted as "E14/E10," colored in blue, Figure 5(middle)) and 47 eV and 115 eV (denoted as "E13/E10," colored in black, Figure 5 (right)) are on top of each other with a maximum value near 0.20, the red line, derived from the distribution of the flux ratio of 27 eV and 115 eV (denoted as "E15/E10," Figure 5 (left)), has a ∼0.05 offset from the other two, with a maximum around 0.15. The possible explanation of this discrepancy is as follows. The spiked fluxes in the 20–30 eV range (partially falls into the 27 eV energy channel), a typical feature of photoelectrons generated by the very intense He II 30.4 nm solar line, can be mixed with lower fluxes at nearby energies due to the energy shift caused by spacecraft potential. *Frahm et al.* [2006a] noted that MEX had a negative spacecraft potential when in the ionosphere, reducing the energy of the production spikes by 5 to 10 eV, which might be happening for MGS as well. A spacecraft potential shift would result into a broader flux distribution of photoelectrons in the 27 eV bin but not influence the other two energy channels nearly as because the typical photoelectron spectrum is rather smooth from 30 to 60 eV. This broadening of photoelectron distribution at 27 eV (wider error bars for the photoelectron population, therefore larger overlapping areas of the two populations in Figure 5 (left)) makes it less distinguishable from the solar wind samples. Therefore, results from the 27 eV energy channel are relatively less trustworthy in this study. The following analysis focuses on one of the other two, the flux ratio of the energy channel pair 36 eV and 115 eV.

Based on the discussions above, it is easy to calculate that the occurrence rate of solar wind electrons in regions where the magnetic field elevation angle is above 45° is around 1/6. In addition, it seems that a flux ratio cutoff can be obtained from this bimodal distribution to isolate solar wind electron samples or photoelectron samples for further use, such as studying the energy flux of each population. For each pair of flux ratios, we define this cutoff for each downward pitch angle bin such that the values from two fitted Gaussian distributions are equal and then use the minimum of these nine cutoffs as the solar wind electron cutoff and the maximum as the photoelectron cutoff. For the flux ratio of 36 eV and 115 eV, the cutoff for the solar wind electrons is 27, the dashed line as shown in Figure 2g, and the cutoff for the photoelectron is 35. For the flux ratio of 47 eV and 115 eV, the two numbers are 14 and 19. These numbers may be used to distinguish photoelectrons and solar wind electrons without examining the energy spectra for future studies.

### 3.3. Occurrence Rate's Dependence on Magnetic Elevation Angles

The occurrence rate of 1/6 is for a large variation of magnetic elevation angles. As mentioned above, the strong crustal magnetic field lines is more likely to be connected to the IMF (i.e., open) when the elevation
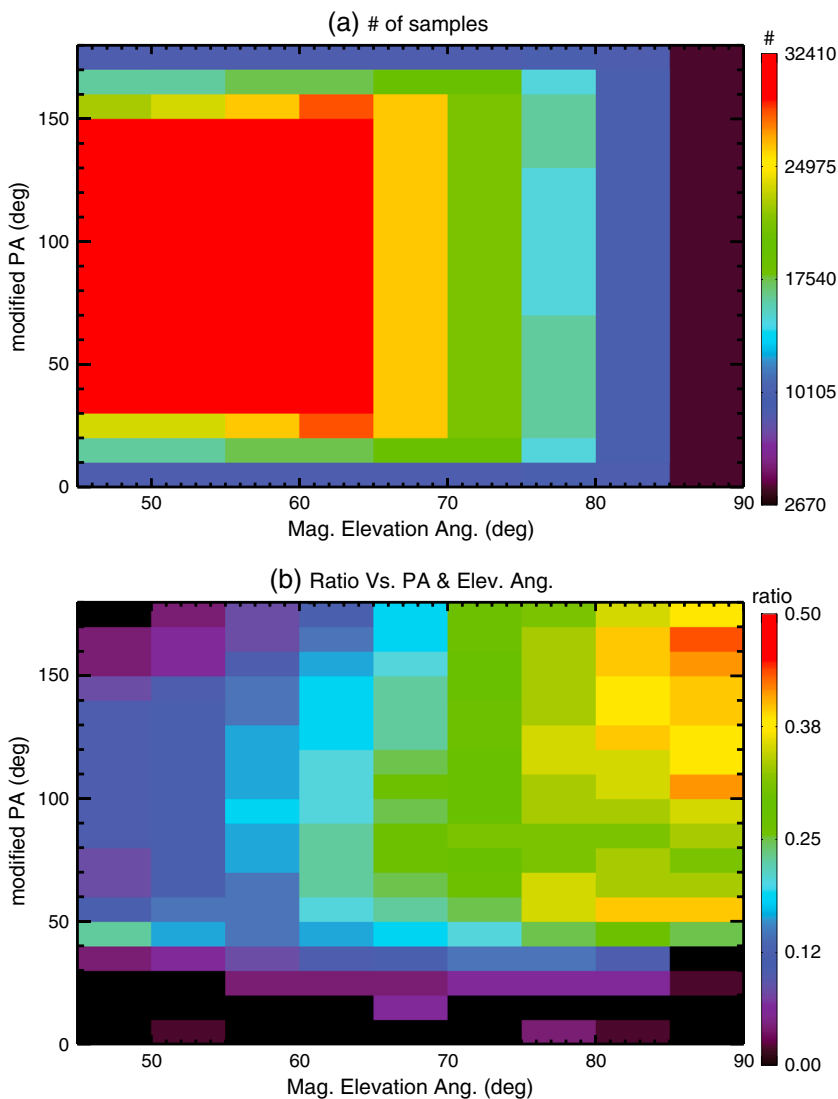
**Figure 7.** (a) The sample number for each pitch angle and magnetic elevation angle bin. (b) The sample ratio of the two populations for each pitch angle and magnetic elevation angle bin.

angles are near 90°, thus a larger chance for solar wind electron precipitation. How the occurrence rates change against magnetic elevation angles is examined here.

The data set is divided into nine magnetic elevation angle bins with a bin size of 5°. For each bin, similar to the previous section, the flux ratio distribution is obtained and then fitted with two Gaussian functions. From the fitting to the distributions, the sample ratio of the solar wind electron and the photoelectron can be determined. The sample number for each PA × Elevation Angle bin (a bin size of 10° × 5°) is shown in Figure 7a and the sample ratio in Figure 7b. As expected, Figure 7a shows large samples near PA 90°, then lower toward PA 0° and 180°. The sample number is about the same for all pitch angles as the elevation angle increases. When the elevation angle is near 90°, magnetic field lines have little horizontal component, thus are mostly in the plane of the instrument and all pitch angles are fully sampled for almost all of the measurements. One thing to notice is that the minimum sample number (colored in black) is 2670 instead of 0. The high sample ratio, up to 0.45, of the solar wind electrons concentrates at high elevation angle bins as shown in Figure 7b. For elevation angles lower than 60°, the sample ratio of solar wind electron to photoelectron is mostly below 0.2. Also, the sample ratio is higher again near PA 90° for low elevation angles. For high elevation angles, where most of the magnetic field lines are open, the sample ratio is higher for downward pitch angles. The observations for upward pitch angles consist of both photoelectrons and

XU ET AL.
10,108
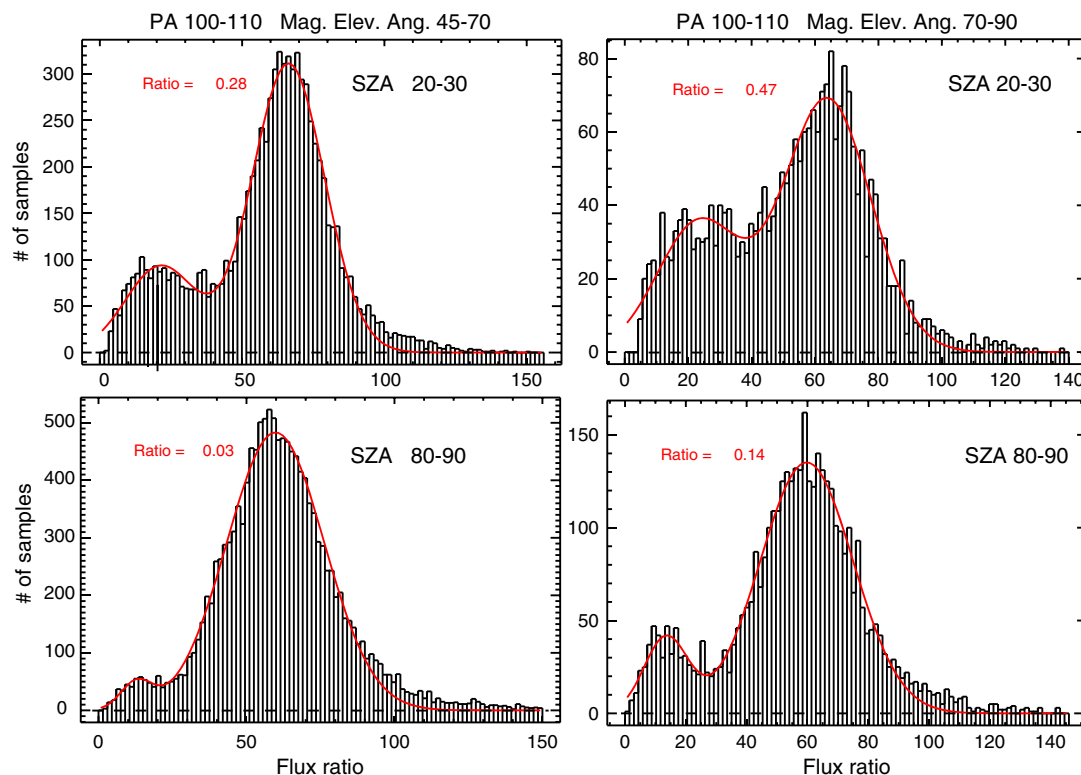
**Figure 8.** The distribution of flux ratio of energy pair 36 eV and 115 eV at different solar zenith angles (SZA) for modified PA 100°–110°. The two figures in the left are for absolute magnetic elevation angle 45°–70° and right for 70°–90°; (top) SZA 20°–30° and (bottom) 80°–90°. Similarly, the red lines are the fittings and the sample ratios of the two populations are shown at the upper left corner.

reflected solar wind electrons, while for downward pitch angles, the sample should be mostly solar wind electrons. In addition, the reflected solar wind electrons can be seen in the upward pitch angles as low as 20°–50° (transition from blue to black in Figure 7b), indicating a loss cone width of about this size.

The fitting function does not perform well when solar wind electron samples are very small. For example, for elevation angle 45°–50° and PA 40°–50° in Figure 7b, the sample ratio (0.24) is unreasonably high for a upward pitch angle bin despite barely being able to see a second population. Also, some of the sample ratios are negative, such as elevation angle 45°−50° and PA 170°−180°. It is because the fitting returns a negative amplitude to one of the two fitted Gaussian distributions. The negative sample ratios are set to 0 in Figure 7b.

From the discussion above, the occurrence rate of solar wind electron precipitation largely varies with magnetic elevation angles, lower than 10% for more horizontal magnetic field lines but as high as 1/3 for vertical field lines. This result is also consistent with Figure 11 of *Brain et al.* [2007]. In between closed magnetic loops, the one-sided loss cone distribution, an indicator of solar wind electron precipitation as well as open magnetic field lines, is the dominant pitch angle distribution.

### 3.4. Occurrence Rate's Dependence on Solar Zenith Angles

Graphically, the occurrence rate of solar wind electron precipitation correlates with magnetic elevation angle because vertical magnetic field lines are more likely to be open. Physically, this rate can vary with the solar zenith angle (SZA) as solar wind normal pressure onto the planet is smaller with increasing SZA. In addition, the altitude of the Martian dayside electron density peak is also roughly proportional to a cosine function of SZA [e.g., *Hantsch and Bauer*, 1990; *Withers*, 2009; *Withers et al.*, 2014], which can be explained by Chapman theory [*Chapman*, 1931a, 1931b]. As a result, the magnetic pileup boundary (MPB) is closer to the planet near the subsolar point and at higher altitudes at larger SZA [e.g., *Vignes et al.*, 2000; *Crider et al.*, 2002; *Nagy et al.*, 2004]. With a higher downward directed solar wind pressure, i.e., a smaller SZA, the IMF can erode more deeply into the Martian atmosphere and connect with strong crustal fields with the
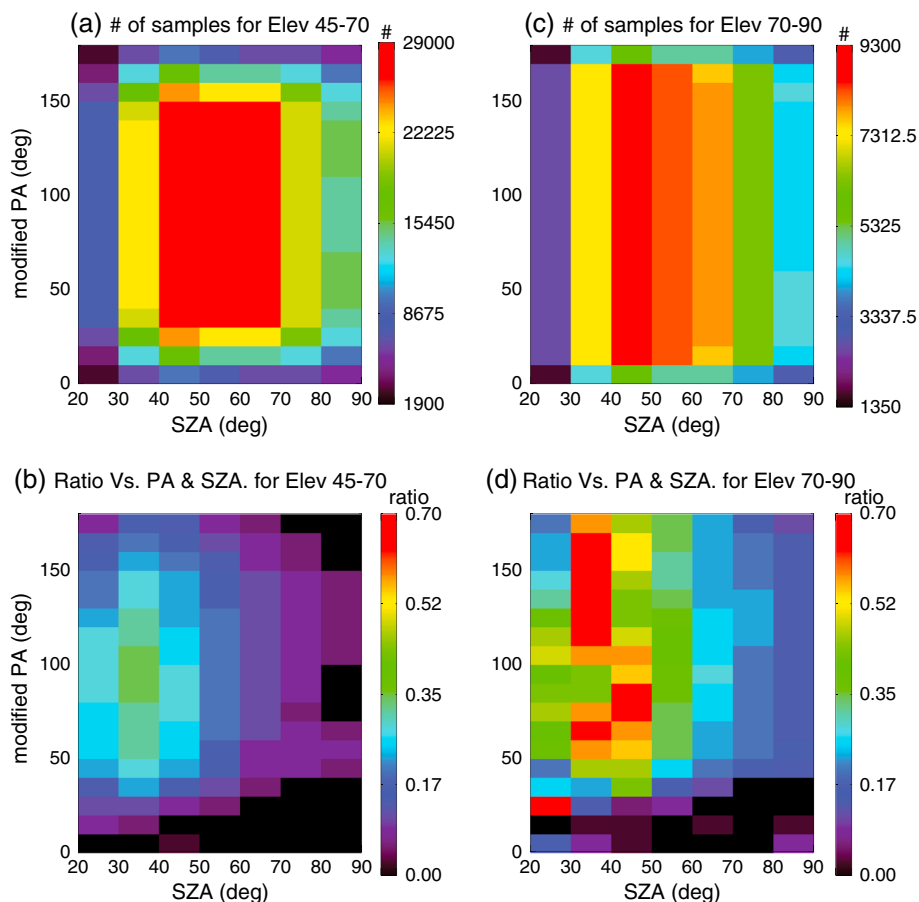
**Figure 9.** The upper two panels are the sample number for each pitch angle and magnetic elevation angle bin for absolute magnetic elevation angle (a) 45°–70° and (c) 70°–90°. The lower two panels are the sample ratio of the two populations for each pitch angle and SZA bin for elevation angle (b) 45°–70° and (d) 70°–90°.

opposite component. To explore this relation, the data set is divided into two magnetic elevation angle groups, absolute value within 45°–70° and within 70°–90°, and then into seven SZA bins of 10°. The minimum SZA is 20° because the measurements were made by MGS at 2 P.M. LT.

Figure 8 shows some histogram examples at PA 100°–110°, the left column for absolute magnetic elevation angle 45°–70° and right for 70°–90°; the upper row for SZA 20°–30° and the lower for 80°–90°. Again, the distribution is bi-modal and the sample ratio derived from the fitting is bigger for large elevation angle by comparing the right column to the left column. For small SZAs (Figure 8, top), the left population, i.e., the solar wind electrons, is of a larger proportion of the total sample than that for large SZAs (Figure 8, bottom), as shown as the sample ratios in the upper left corner of each panel. As expected, the occurrence rate of the solar wind electron precipitation is higher with smaller SZA.

To better examine all the pitch angles, Figure 9 shows the sample number (a and c) and sample ratio (b and d) for the two magnetic elevation angle groups, respectively. Because that data set is confined in the geographic box as said in the methodology section, the high sample number concentrates in mid-SZA and PA ~90°. On one hand, for each group, the ratios in Figure 9d, where magnetic field lines are more vertical, are generally much higher than in Figure 9b, as expected. On the other hand, for both Figures 9b and 9d, one common feature is the higher ratio for smaller SZAs than larger SZAs. Also, the maximum ratio now increases to 0.7, which means a maximum occurrence rate of 41%. The pitch angle dependence can also be explained by the three possibilities described in section 1. Note that the few high ratios in PA < 40° and SZA 20°–30° are caused by the ill fittings.

Another common feature in Figures 9b and 9d is that the highest ratio surprisingly occurs at SZA 30°–40° instead of 20°–30°. Through the examination of the magnetic elevation angle against latitude, as shown
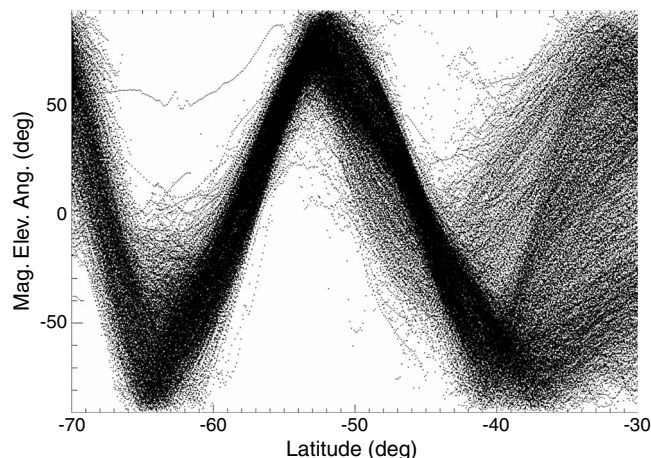
**Figure 10.** Magnetic elevation angle against latitude.

in Figure 10, it is found that the magnetic loop of north latitude −30° to −40°, where most of the SZA 20°–30° measurement comes from, has more random magnetic elevation angles than other latitudes. In other words, the magnetic field lines for SZA 20°–30° might be of more random directions and less likely connect to the IMF.

From Figure 4, a seasonal change of low flux ratio population, i.e., solar wind electrons, is seen in the left column, being denser in the summer and sparser in the winter, as expected. This seasonal feature can be explained by the SZA dependence. Because MGS is locked to 2 P.M. LT on the dayside and the tilt of Mars is around 25°, the alternating bar-like strong crustal fields, i.e., the geography box used to select data, are concentrated at low SZAs in the southern summer and high SZAs in the winter. It means that there is a higher chance to see solar wind electrons in the southern summer than winter. Generally speaking, even without locking a particular local time but just due to the tilt of Mars, the strong crustal fields can reach a lower SZA in the summer, leading to more solar wind electron precipitation. Furthermore, Mars is closer to the Sun during the southern summer, a higher dynamic pressure at the subsolar point is also expected, likely causing more reconnection between the IMF and the crustal fields. All considered, a seasonal variation of solar wind electron precipitation is expected.

### 3.5. Energy Deposition

The identification of solar wind electrons, the occurrence rate and its dependence on the magnetic elevation angle and also solar zenith angle are discussed in the above sections. In this section, we will discuss these superthermal electrons' energy depositions into the Martian atmosphere, which can cause localized heating, excitation and dissociation, and ionization.

The first step is to isolate solar wind electron samples. As mentioned in section 3.2, the minimum flux ratio cutoff of nine downward PAs, 90°–180°, can be used to select solar wind electron precipitation events. To make this selection more strictly, the minimum cutoffs of two energy pairs, 27 for 36 eV and 115 eV and 15 for 47 eV and 115 eV, are both applied. Due to the small samples at PA near 0° and 180°, as shown in Figure 7a, the cutoff criteria is applied to downward PA 90°–170° and 90°–180°, separately. Even though the selected sample numbers of solar wind electron precipitation events for the two cases vary by a factor of two, (11374 and 5935, respectively), the results, such as the distributions and the number/energy fluxes, are actually quite similar. Hence, the results of the first case, filtered by only PA 90°–170°, are shown in Figure 11. The left column is for pitch angle-averaged number flux distributions, while the right column is for energy flux distributions. From top to bottom, each row is the downward, upward, and net (downward subtracting upward) flux, respectively. For the upward/reflected solar wind electron fluxes, the cutoff criterion is applied again to ensure excluding the photoelectrons. Also, the average (denoted as "mean"), median, and mode values are listed in each plot.

As shown in Figure 11, take the median values as examples, the precipitating solar wind electron number and energy fluxes are $1.02 \times 10^8$ cm$^{-2}$ s$^{-1}$ and $3.24 \times 10^9$ eV cm$^{-2}$ s$^{-1}$, respectively. However, $\sim 60\%$ of the incoming fluxes are reflected back to the MGS altitude by magnetic focusing and/or collisions, as shown in Figures 11b and 11e. We have further investigated the reflection of solar wind electrons. First, the percentage of the reflected out of the total solar wind electron samples varies with different upward pitch angles, $> 90\%$ for PA greater than 40° and $< 30\%$ for PA smaller than 20°. In other words, more field-aligned solar wind electrons are of higher chance to deposit their energy into the upper atmosphere, as expected. Then, for electrons with energy lower than 100 eV, around 60% of the incoming energy flux is reflected while for energy above 100 eV, it is around 70%. On one hand, the reflection is about the same for these
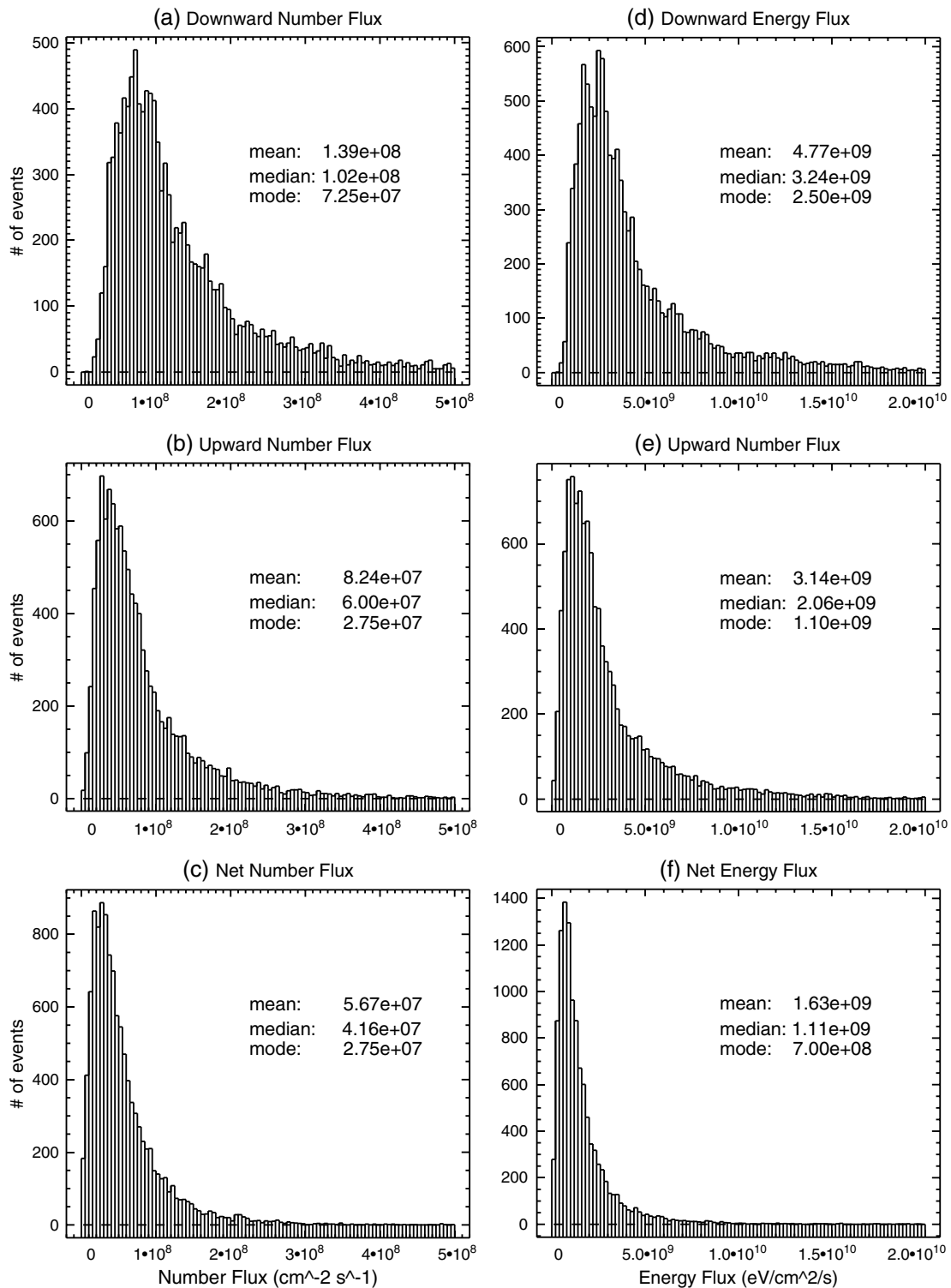
**Figure 11.** The distributions of solar wind electron fluxes: (a) downward number fluxes, (b) upward number fluxes, (c) net number fluxes, (d) downward energy fluxes, (e) upward energy fluxes, and (f) net energy fluxes. The average, median, and mode values of each distribution are also shown in the upper right corner.

different energy ranges, which implies that the magnetic focusing is the dominant process. On the other hand, the high-energy electrons are more likely to be reflected, which maybe result from the lower collision cross sections ($\propto 1/E^2$). It also means that collisions also play a relatively minor role in the reflection.

With so much energy reflected, the number/energy fluxes absorbed by the atmosphere down below 400 km are only the net part, a median value of $4.16 \times 10^8$ cm$^{-2}$ s$^{-1}$ and $1.11 \times 10^9$ eV cm$^{-2}$ s$^{-1}$ for the number and energy flux, respectively. To compare it with solar photon input, the authors have calculated the solar flux based on the Flare Irradiance Spectral Model [*Chamberlin et al.*, 2007, 2008]. The EUV irradiance is integrated from 1 to 100 nm, and the resulting solar EUV flux is then scaled to Mars orbit, along with a time shift based on a point-by-point basis (assuming a 27 day solar rotation) to account for the different orbital positions of Earth and Mars, similar to the method used in *Mitchell et al.* [2001]. The mean EUV flux from January 1999 to January 2007 (roughly the same time period of the MGS data set used in this study) is around $1.9 \times 10^{-7}$ W/cm$^2$, or $1.2 \times 10^{12}$ eV cm$^{-2}$ s$^{-1}$. It means that the energy flux deposition of solar wind electrons into the Martian atmosphere is about 0.1% of the solar photon absorption. However, this 0.1% may need some adjustment. First, unlike solar EUV fluxes that only vary within a factor of 2, the long tails in the flux distributions are seen in Figure 11 and under extreme cases, the energy input from solar wind electrons can be 10 times larger. Also, the estimated solar EUV flux does not include the effect of solar zenith angles, which may drop by a factor of 2 at SZA greater than 60°.

This direct comparison between the energy input of these two sources seemingly suggests that the energy deposition of the solar wind electrons is insignificant. However, the deposition processes of these two energy sources are quite different. It is possible that solar wind electrons can cause significant changes locally. In fact, through a closer examination of the contribution of the net energy fluxes from electrons with energy lower and higher than 100 eV individually, the former is twice that of the energy flux deposition of the latter. Notice that low-energy electrons are more likely to cause heating at higher altitudes instead of ionization at lower altitudes. Therefore, it is possible that these solar wind electrons can efficiently heat the cusps. Further study of this energy deposition and possible influence on the upper atmosphere requires modeling.

One thing not addressed in the previous analysis is the possible contamination by spacecraft photoelectrons and other secondary electrons. The anode sectors (sectors 5–12) of MGS ER more likely to detect these spacecraft electrons look toward zenith and along the spacecraft bus [*Mitchell et al.*, 2001; *Xu et al.*, 2014]. Since the data set of this study is confined to more vertical magnetic fields lines, these contaminated sectors are converted into upward modified pitch angles while the downward modified pitch angles should be barely affected. Hence, the possible contamination may not significantly influence most of the previous analysis. However, the reflected energy flux (in upward pitch angles) here might be overestimated because of the contamination. As a result, the different reflection of high- and low-energy electrons might be partly or even entirely due to the contamination. In addition, it also leads to an underestimation of solar wind electron energy deposition. The actual energy deposition should range from the net energy flux, $1.11 \times 10^9$ eV cm$^{-2}$ s$^{-1}$, to the downward energy flux (assuming all the upward energy fluxes are contaminations from spacecraft electrons), $3.24 \times 10^9$ eV cm$^{-2}$ s$^{-1}$. This upper bound of energy deposition also increases the percentage relevant to the solar input to 0.3% and more than 2% under extreme cases.

## 4. Discussion and Conclusions

In this study, the knee feature near 60 eV in the photoelectron energy spectra is utilized to differentiate the solar wind/magnetosheath electrons from the ionospheric photoelectrons. The flux ratio of one energy channel lower than 60 eV and one higher, such as 36 eV and 115 eV, is calculated for the selected data set, the nearly 8 year measurements of MGS MAG/ER over a specific dayside strong crustal field region. The distribution of the flux ratios is bimodal, which implies the existence of a second population other than photoelectrons, i.e., the solar wind/magnetosheath electrons.

Then a curve fitting that consists of two Gaussian functions is applied, through which the occurrence rate of dayside solar wind electron precipitation through the cusps over the strong crustal fields is determined. For magnetic elevation angles greater than 45°, the occurrence rate is about 1/6. Furthermore, by dividing data into nine magnetic elevation angle bins, the occurrence rate increases with the magnetic elevation angle, as expected. The maximum occurrence rate is 1/3, when the magnetic field lines are nearly vertical.

The results have shown that the occurrence rate is lower at larger solar zenith angles, probably resulting from the higher altitude of MPB due to a smaller normal solar wind dynamic pressure and also a flared away ionosphere near terminators. A maximum occurrence rate of 40% is found, which suggests two things. First, the reconnected/open magnetic fields are more likely near the subsolar point. Second, even for vertical magnetic field lines with small SZA, the chance is surprisingly high that the magnetic field is still closed at 400 km. Due to the tilt and the orbital position of Mars, a seasonal variation of the precipitation is also expected and found. In other words, during the southern summer (winter), the solar wind precipitation occurs more (less) often. The occurrence rates presented here can roughly be approximated as how often the IMF is connected to strong crustal fields at 400 km. However, be aware that this rate may count in occasions when a draped field line moves to 400 km, even though this is very rare near the strong crustal fields [*Brain et al.*, 2005, 2007], and also the transit of solar wind/magnetosheath electron samples on closed magnetic field lines right at when the reconnection between the IMF and strong crustal fields happens. In addition, this occurrence rate probably varies with altitude as the cusps expand in area with increasing altitude.

Open magnetic field lines also mean the particles and energy exchange between the Martian atmosphere and the solar wind. The energy flux input from solar wind electron precipitation is also investigated and is found to be roughly 0.1% up to 2% of the solar EUV flux input to the Martian atmosphere. However, this simple comparison does not take into account the effects of the solar zenith angle or the different deposition processes. The localized effects of the solar wind electrons might be significant. The energy deposition of the solar wind electrons, especially the heating rates, at different altitudes and SZAs can be further studied by modeling, such as the multistream superthermal electron transportation model [*Khazanov and Liemohn*, 1995; *Liemohn et al.*, 1997, 2003, 2006]. Furthermore, the magnetic fields in the Martian northern hemisphere, where the crustal fields are weak, are more likely to be draped. The solar wind electrons may have access to the atmosphere through these draped fields lines and deposit their energy at some altitude range through collision with the neutral particles and/or ions. *Gan et al.* [1990] conducted a study on how the solar wind superthermal electrons affect the electron temperature near the ionopause on Venus. Their results suggested that except for solar EUV heating, the additional heating from the energy deposition of solar wind electron fluxes moving along the magnetic field lines was also needed to explain the high-electron temperature in the magnetized upper ionosphere and in the mantle region on Venus. However, few studies have been conducted on the heating effect of solar wind electrons, which may deposit energy into the Martian upper atmosphere while moving along the draped magnetic field lines. Further investigations of this potential heat source are needed to have a better understanding of Martian atmosphere.

## References

Acuña, M., et al. (1992), Mars observer magnetic fields investigation, *J. Geophys. Res.*, *97*(E5), 7799–7814.

Acuña, M., et al. (1998), Magnetic field and plasma observations at Mars: Initial results of the Mars Global Surveyor mission, *Science*, *279*(5357), 1676–1680.

Barabash, S., et al. (2006), The analyzer of space plasmas and energetic atoms (ASPERA-3) for the Mars express mission, *Space Sci. Rev.*, *126*(1–4), 113–164.

Bertaux, J.-L., F. Leblanc, O. Witasse, E. Quemerais, J. Lilensten, S. Stern, B. Sandel, and O. Korablev (2005), Discovery of an aurora on Mars, *Nature*, *435*(7043), 790–794.

Brain, D., F. Bagenal, M. Acuña, and J. Connerney (2003), Martian magnetic morphology: Contributions from the solar wind and crust, *J. Geophys. Res.*, *108*(A12), 1424, doi:10.1029/2002JA009482.

Brain, D., J. Halekas, R. Lillis, D. Mitchell, R. Lin, and D. Crider (2005), Variability of the altitude of the Martian sheath, *Geophys. Res. Lett.*, *32*, L18203, doi:10.1029/2005GL023126.

Brain, D., J. Halekas, L. Peticolas, R. Lin, J. Luhmann, D. Mitchell, G. Delory, S. Bougher, M. Acuña, and H. Rème (2006), On the origin of aurorae on Mars, *Geophys. Res. Lett.*, *33*, L01201, doi:10.1029/2005GL024782.

Brain, D., R. Lillis, D. Mitchell, J. Halekas, and R. Lin (2007), Electron pitch angle distributions as indicators of magnetic field topology near Mars, *J. Geophys. Res.*, *112*, A09201, doi:10.1029/2007JA012435.

Brain, D., A. Baker, J. Briggs, J. Eastwood, J. Halekas, and T.-D. Phan (2010), Episodic detachment of Martian crustal magnetic fields leading to bulk atmospheric plasma escape, *Geophys. Res. Lett.*, *37*, L14108, doi:10.1029/2010GL043916.

Chamberlin, P. C., T. N. Woods, and F. G. Eparvier (2007), Flare irradiance spectral model (FISM): Daily component algorithms and results, *Space Weather*, *5*, S07005, doi:10.1029/2007SW000316.

Chamberlin, P. C., T. N. Woods, and F. G. Eparvier (2008), Flare irradiance spectral model (FISM): Flare component algorithms and results, *Space Weather*, *6*, S05001, doi:10.1029/2007SW000372.

Chapman, S. (1931a), The absorption and dissociative or ionizing effect of monochromatic radiation in an atmosphere on a rotating Earth, *Proc. Phys. Soc.*, *43*, 26–45, doi:10.1088/0959-5309/43/1/305.

Chapman, S. (1931b), The absorption and dissociative or ionizing effect of monochromatic radiation in an atmosphere on a rotating earth—Part II. Grazing incidence, *Proc. Phys. Soc.*, *43*, 483–501, doi:10.1088/0959-5309/43/5/302.

Connerney, J., M. Acuña, N. Ness, G. Kletetschka, D. Mitchell, R. Lin, and H. Reme (2005), Tectonic implications of Mars crustal magnetism, *Proc. Natl. Acad. Sci. U.S.A.*, *102*(42), 14,970–14,975.

Crider, D., et al. (2000), Evidence of electron impact ionization in the magnetic pileup boundary of Mars, *Geophys. Res. Lett.*, *27*(1), 45–48, doi:10.1029/1999GL003625.

Crider, D. H., et al. (2002), Observations of the latitude dependence of the location of the Martian magnetic pileup boundary, *Geophys. Res. Lett.*, *29*(8), 1170, doi:10.1029/2001GL013860.

Dubinin, E., M. Fraenz, J. Woch, J. Winnigham, R. Frahm, R. Lundin, and S. Barabash (2008a), Suprathermal electron fluxes on the nightside of Mars: ASPERA-3 observations, *Planet. Space Sci.*, *56*(6), 846–851, doi:10.1016/j.pss.2007.12.010.

Dubinin, E. M., M. Fraenz, J. Woch, E. Roussos, J. D. Winningham, R. A. Frahm, A. Coates, F. Leblanc, R. Lundin, and S. Barabash (2008b), Access of solar wind electrons into the Martian magnetosphere, *Ann. Geophys.*, *26*(11), 3511–3524, doi:10.5194/angeo-26-3511-2008.

Fox, J. L., and A. Dalgarno (1979), Ionization, luminosity, and heating of the upper atmosphere of Mars, *J. Geophys. Res.*, *84*(A12), 7315–7333.

Frahm, R., et al. (2006a), Carbon dioxide photoelectron energy peaks at Mars, *Icarus*, *182*(2), 371–382.

Frahm, R., et al. (2006b), Locations of atmospheric photoelectron energy peaks within the Mars environment, *Space Sci. Rev.*, *126*(1–4), 389–402.

Gan, L., T. Cravens, and M. Horanyi (1990), Electrons in the ionopause boundary layer of Venus, *J. Geophys. Res.*, *95*(A11), 19,023–19,035.

Hantsch, M., and S. Bauer (1990), Solar control of the Mars ionosphere, *Planet. Space Sci.*, *38*(4), 539–542.

Harnett, E. M., and R. M. Winglee (2005), Three-dimensional fluid simulations of plasma asymmetries in the Martian magnetotail caused by the magnetic anomalies, *J. Geophys. Res.*, *110*, A07226, doi:10.1029/2003JA010315.

Khazanov, G., and M. Liemohn (1995), Nonsteady state ionosphere-plasmasphere coupling of superthermal electrons, *J. Geophys. Res.*, *100*(A6), 9669–9681.

Krymskii, A., T. Breus, N. Ness, M. Acuña, J. Connerney, D. Crider, D. Mitchell, and S. Bauer (2002), Structure of the magnetic field fluxes connected with crustal magnetization and topside ionosphere at Mars, *J. Geophys. Res.*, *107*(A9), 1245, doi:10.1029/2001JA000239.

Krymskii, A., T. Breus, N. Ness, D. Hinson, and D. Bojkov (2003), Effect of crustal magnetic fields on the near terminator ionosphere at Mars: Comparison of in situ magnetic field measurements with the data of radio science experiments on board Mars Global Surveyor, *J. Geophys. Res.*, *108*(A12), 1431, doi:10.1029/2002JA009662.

Krymskii, A., N. Ness, D. Crider, T. Breus, M. Acuña, and D. Hinson (2004), Solar wind interaction with the ionosphere/atmosphere and crustal magnetic fields at Mars: Mars global surveyor magnetometer/electron reflectometer, radio science, and accelerometer data, *J. Geophys. Res.*, *109*, A11306, doi:10.1029/2004JA010420.

Leblanc, F., et al. (2008), Observations of aurorae by SPICAM ultraviolet spectrograph on board Mars Express: Simultaneous ASPERA-3 and MARSIS measurements, *J. Geophys. Res.*, *113*, A08311, doi:10.1029/2008JA013033.

Liemohn, M., G. Khazanov, T. Moore, and S. Guiter (1997), Self-consistent superthermal electron effects on plasmaspheric refilling, *J. Geophys. Res.*, *102*(A4), 7523–7536.

Liemohn, M. W., D. L. Mitchell, A. F. Nagy, J. L. Fox, T. W. Reimer, and Y. Ma (2003), Comparisons of electron fluxes measured in the crustal fields at mars by the mgs magnetometer/electron reflectometer instrument with a b field–dependent transport code, *J. Geophys. Res.*, *108*(E12), 5134, doi:10.1029/2003JE002158.

Liemohn, M. W., et al. (2006), Numerical interpretation of high-altitude photoelectron observations, *Icarus*, *182*(2), 383–395.

Liemohn, M. W., Y. Ma, R. A. Frahm, X. Fang, J. U. Kozyra, A. F. Nagy, J. D. Winningham, J. R. Sharber, S. Barabash, and R. Lundin (2007), Mars global MHD predictions of magnetic connectivity between the dayside ionosphere and the magnetospheric flanks, in *The Mars Plasma Environment*, pp. 63–76, Springer, New York.

Lillis, R. J., and D. A. Brain (2013), Nightside electron precipitation at mars: Geographic variability and dependence on solar wind conditions, *J. Geophys. Res. Space Physics*, *118*, 3546–3556, doi:10.1002/jgra.50171.

Ma, Y. J., X. Fang, A. F. Nagy, C. T. Russell, and G. Toth (2014), Martian ionospheric responses to dynamic pressure enhancements in the solar wind, *J. Geophys. Res. Space Physics*, *119*, 1272–1286, doi:10.1002/2013JA019402.

Mantas, G. P., and W. B. Hanson (1979), Photoelectron fluxes in the Martian ionosphere, *J. Geophys. Res.*, *84*(A2), 369–385, doi:10.1029/JA084iA02p00369.

Mitchell, D., R. Lin, C. Mazelle, H. Reme, P. Cloutier, J. Connerney, M. Acuña, and N. Ness (2001), Probing Mars' crustal magnetic field and ionosphere with the MGS electron reflectometer, *J. Geophys. Res.*, *106*(E10), 23,419–23,427.

Nagy, A., et al. (2004), The plasma environment of Mars, in *Mars Magnetism and Its Interaction with the Solar Wind*, pp. 33–114, Springer, Netherlands.

Nielsen, E., et al. (2007), Local plasma processes and enhanced electron densities in the lower ionosphere in magnetic cusp regions on Mars, *Planet. Space Sci.*, *55*(14), 2164–2172.

Schunk, R., and A. Nagy (2000), *Ionospheres: Physics, Plasma Physics, and Chemistry, Cambridge Atmospheric and Space Science Series, 59*, Cambridge Univ. Press, New York.

Trantham, M., M. Liemohn, D. Mitchell, and J. Frank (2011), Photoelectrons on closed crustal field lines at Mars, *J. Geophys. Res.*, *116*, A07311, doi:10.1029/2010JA016231.

Vignes, D., C. Mazelle, H. Rme, M. H. Acuña, J. E. P. Connerney, R. P. Lin, D. L. Mitchell, P. Cloutier, D. H. Crider, and N. F. Ness (2000), The solar wind interaction with Mars: Locations and shapes of the bow shock and the magnetic pile-up boundary from the observations of the MAG/ER Experiment onboard Mars Global Surveyor, *Geophys. Res. Lett.*, *27*, 49–52, doi:10.1029/1999GL010703.

Withers, P. (2009), A review of observed variability in the dayside ionosphere of Mars, *Adv. Space Res.*, *44*, 277–307, doi:10.1016/j.asr.2009.04.027.

Withers, P., M. Mendillo, H. Rishbeth, D. Hinson, and J. Arkani-Hamed (2005), Ionospheric characteristics above Martian crustal magnetic anomalies, *Geophys. Res. Lett.*, *32*, L16204, doi:10.1029/2005GL023483.

Withers, P., K. Fallows, and M. Matta (2014), Predictions of electron temperatures in the Mars ionosphere and their effects on electron densities, *Geophys. Res. Lett.*, *41*, 2681–2686, doi:10.1002/2014GL059683.

Xu, S., M. W. Liemohn, D. L. Mitchell, and M. D. Smith (2014), Mars photoelectron energy and pitch angle dependence on intense lower atmospheric dust storms, *J. Geophys. Res. Planets*, *119*, 1689–1706, doi:10.1002/2013JE004594.